

Photon-fusion reactions from the chiral Lagrangian with dynamical light vector mesons

I.V. Danilkin^{1,3}, M.F.M. Lutz¹, S. Leupold², C. Terschläsen²

¹ GSI Helmholtzzentrum für Schwerionenforschung GmbH,
Planckstraße 1, 64291 Darmstadt, Germany

² Institutionen för fysik och astronomi, Uppsala Universitet, Box 516, 75120 Uppsala, Sweden

³ SSC RF ITEP, Bolshaya Chermushkinskaya 25, 117218 Moscow, Russia

the date of receipt and acceptance should be inserted later

Abstract We study the reactions $\gamma\gamma \rightarrow \pi^0\pi^0, \pi^+\pi^-, K^0\bar{K}^0, K^+K^-, \eta\eta$ and $\pi^0\eta$ based on a chiral Lagrangian with dynamical light vector mesons as formulated within the hadrogenesis conjecture. At present our chiral Lagrangian contains 5 unknown parameters that are relevant for the photon fusion reactions. They parameterize the strength of interaction terms involving two vector meson fields. These parameters are fitted to photon fusion data $\gamma\gamma \rightarrow \pi^0\pi^0, \pi^+\pi^-, \pi^0\eta$ and to the decay $\eta \rightarrow \pi^0\gamma\gamma$. In order to derive gauge invariant reaction amplitudes in the resonance region constraints from micro-causality and exact coupled-channel unitarity are used. Our results are in good agreement with the existing experimental data from threshold up to about 0.9 GeV for the two-pion final states. The a_0 meson in the $\pi^0\eta$ channel is dynamically generated and an accurate reproduction of the $\gamma\gamma \rightarrow \pi^0\eta$ data is achieved up to 1.2 GeV. Based on our parameter sets we predict the $\gamma\gamma \rightarrow K^0\bar{K}^0, K^+K^-, \eta\eta$ cross sections.

Keywords Meson production · Chiral Lagrangians · Vector-meson dominance · Partial-wave analysis · Dispersion relations

PACS 13.60.Le · 12.39.Fe · 12.40.Vv · 11.80.Et · 11.55.Fv

1 Introduction

Photon-fusion reactions $\gamma\gamma \rightarrow PP$ (with $PP = \pi^0\pi^0, \pi^+\pi^-, K^0\bar{K}^0, K^+K^-, \eta\eta$ and $\pi^0\eta$) play an important role in our understanding of non-perturbative QCD [1, 2, 3, 4, 5]. As a systematic approach chiral perturbation theory (χ PT) is applied to describe these reactions at low energies [6, 7]. Such studies have been performed at next-to-leading order (one loop) [8, 9] and at next-to-next-to-leading order (two loops) [7, 6]. However, χ PT

is limited to the near-threshold region and cannot serve as an appropriate framework in the resonance region, where exact coupled-channel unitarity becomes an important issue. In [10, 11, 12, 13] it was shown that the combination of electromagnetic gauge invariance, micro-causality and coupled-channel unitarity together with chiral symmetry helps to achieve a systematic approximation of hadron interactions beyond the threshold region. In the following the same approach is applied to the photon-fusion reactions.

The cross sections of fusion processes are very sensitive to hadronic final-state interactions. Therefore, a crucial input for the present work is a proper description of the reactions of two pseudoscalars into the same or different two pseudoscalars. Recently, within the novel unitarization approach developed in [10, 11, 13] a coupled-channel computation of Goldstone-boson scattering has been performed [12]. The calculations are based on the chiral Lagrangian formulated with light vector mesons.

The light vector mesons play a crucial role in the hadrogenesis conjecture [14, 15, 16, 17, 18, 19, 20]. Together with the Goldstone bosons they are identified to be the “quasi-fundamental” hadronic degrees of freedom that are expected to generate the meson spectrum. For instance it was shown that the leading chiral interaction of Goldstone bosons with the light vector mesons generates an axial-vector meson spectrum that is quite close to the empirical one [15]. It seems quite natural to keep vector mesons as explicit degrees of freedom when aiming for a description of hadron physics in the resonance region. In particular, this extends the resonance-saturation mechanism [21] by taking into account explicitly the dynamics of the vector-meson propagator [22]. In the present analysis we further emphasize the significant role of light vector mesons in hadron physics.

One important aspect in photon-fusion reactions is the formation of scalar and tensor resonances. In particular one finds the rather narrow scalar states $a_0(980)$ and $f_0(980)$ [23,1,5]. In the present work we concentrate on energies below 1.2 GeV. There the scalar resonances $f_0(980)$ and $a_0(980)$ appear to dominate. In the approach of [12] both states are dynamically generated from coupled-channel interactions, in accordance with the hadrogenesis conjecture. The two-pion channel, where the $f_0(980)$ resonance is seen prominently, has been discussed in detail in [12]. In contrast, the $\pi\eta$ channel with the $a_0(980)$ state has not been addressed in [12]. There are no elastic $\pi\eta$ scattering data available. However, the $\pi\eta$ channel can be populated by the inelastic photon-fusion reaction. We will show in the following that the dynamical generation of the $a_0(980)$ is in very good agreement with the available experimental data on the photon-fusion production of $\pi\eta$.

At higher energies tensor resonances come into play. In principle, also the tensor resonances $f_2(1270)$ and $a_2(1320)$ are expected to be naturally generated within our approach from vector-vector interactions. However, we focus in the present paper on lower energies and on the mutual interactions between Goldstone bosons. In the present approach vector mesons appear as exchange particles, but not as states in the coupled channels, i.e. we consider scattering and rescattering of the type $\gamma\gamma \rightarrow PP$ and $PP \rightarrow PP$, respectively, but disregard $PP \leftrightarrow VV$, VP , where V generically denotes a vector-meson state. In principle, the basis for the systematic inclusion of vector mesons as coupled-channel states has been laid out in [24]. This technically more challenging computation is beyond the scope of the present work. Consequently the analysis of the resonances $f_2(1270)$ and $a_2(1320)$ and the corresponding energy regime is postponed to the future.

Experimental information on the reactions $\gamma\gamma \rightarrow$ hadrons is accessible in e^+e^- collisions via the reaction $e^+ + e^- \rightarrow e^+ + e^- + \text{hadrons}$ [25,26,27,28,29,30,31]. Recently high-statistics data have been reported by the Belle Collaboration [32,33,34,35], including the first measurement of $\eta\eta$ production. The reaction $\gamma\gamma \rightarrow \pi^0\eta$ is linked to the decay $\eta \rightarrow \pi^0\gamma\gamma$ by crossing symmetry. Recent analyses of this decay have been performed at AGS [36,37] and at MAMI [36,38]. We will use the corresponding integrated and differential information about this decay to constrain our so-far unknown coupling constants parameterizing the strength of interaction terms with two vector meson fields.

The main purpose of this paper is to obtain a unified description of the reactions $\gamma\gamma \rightarrow \pi^0\pi^0$, $\pi^+\pi^-$, $K^0\bar{K}^0$, K^+K^- , $\eta\eta$ and $\pi^0\eta$ using the dispersive effective field theory framework of [10,11,12,13]. The present study

extends the analysis of Goldstone-boson scattering performed in [12]. In the next section we will specify our Lagrangian and comment on the determination of the corresponding coupling constants. Section 3 presents the required decomposition into partial-wave amplitudes. The unitary and causal summation scheme, which is at the heart of the coupled-channel dynamics, is reviewed in section 4. Numerical results and comparisons to data are given in section 5 and a summary of our work is provided in section 6.

2 Chiral interaction Lagrangian including vector mesons

The study of the photon-fusion processes is performed in application of the chiral Lagrangian with explicit vector mesons. The leading order terms of this Lagrangian have been constructed based on a formal power counting scheme [20,19]. The counting rests on the dynamical assumption of hadrogenesis and on large- N_c arguments, where N_c denotes the number of colors. In previous successful applications two- and three-body decays of vector mesons have been presented in [19,39,40]. For photon-fusion reactions the relevant part of the leading-order Lagrangian takes the simple form¹

$$\begin{aligned}
\mathcal{L} = & -\frac{e^2}{2} A^\mu A_\mu \text{tr} \{ \Phi Q [\Phi, Q]_- \} \\
& + i \frac{e}{2} A^\mu \text{tr} \{ \partial_\mu \Phi [Q, \Phi]_- \} \\
& - e f_V \partial_\mu A_\nu \text{tr} \{ \Phi^{\mu\nu} Q \} \\
& - i \frac{f_V h_P}{8 f^2} \text{tr} \{ \partial_\mu \Phi \Phi^{\mu\nu} \partial_\nu \Phi \} \\
& + \frac{e f_V}{8 f^2} \partial_\mu A_\nu \text{tr} \{ \Phi^{\mu\nu} [\Phi, [\Phi, Q]_-]_- \} \\
& + \frac{e f_V h_P}{8 f^2} A_\nu \text{tr} \{ [\partial_\mu \Phi, \Phi^{\mu\nu}]_- [Q, \Phi]_- \} \\
& - \frac{1}{16 f^2} \text{tr} \{ \partial^\mu \Phi_{\mu\alpha} [[\Phi, \partial_\nu \Phi]_-, \Phi^{\nu\alpha}]_- \} \\
& - \frac{b_D}{64 f^2} \text{tr} \{ \Phi^{\mu\nu} \Phi_{\mu\nu} [\Phi, [\Phi, \chi_0]_+]_+ \} \\
& - \frac{g_1}{32 f^2} \text{tr} \{ [\Phi_{\mu\nu}, \partial_\alpha \Phi]_+ [\partial^\alpha \Phi, \Phi^{\mu\nu}]_+ \} \\
& - \frac{g_2}{32 f^2} \text{tr} \{ [\Phi_{\mu\nu}, \partial_\alpha \Phi]_- [\partial^\alpha \Phi, \Phi^{\mu\nu}]_- \} \\
& - \frac{g_3}{32 f^2} \text{tr} \{ [\partial_\mu \Phi, \partial^\nu \Phi]_+ [\Phi_{\nu\tau}, \Phi^{\mu\tau}]_+ \} \\
& - \frac{g_5}{32 f^2} \text{tr} \{ [\Phi^{\mu\tau}, \partial_\mu \Phi]_- [\Phi_{\nu\tau}, \partial^\nu \Phi]_- \}
\end{aligned} \tag{1}$$

¹Note that in [12,19] slightly different notations were used. The relations between e_V , g_D , g_F , h_P in [12,19] — denoted by *old* — and f_V , g_1 , g_2 , h_P used here and in [20] are $f_V = \frac{0.776 \text{ GeV}}{4e} e_V$, $g_1 = g_D$, $g_2 = g_F$ and $h_P = \frac{0.776 \text{ GeV}}{f_V} h_P[\text{old}]$.

$$\begin{aligned}
& -\frac{h_A}{16f} \epsilon_{\mu\nu\alpha\beta} \text{tr} \{ [\Phi^{\mu\nu}, \partial_\tau \Phi^{\tau\alpha}]_+ \partial^\beta \Phi \} \\
& -\frac{b_A}{16f} \epsilon_{\mu\nu\alpha\beta} \text{tr} \{ [\Phi^{\mu\nu}, \Phi^{\alpha\beta}]_+ [\chi_0, \Phi]_+ \} \\
& -\frac{h_O}{16f} \epsilon_{\mu\nu\alpha\beta} \text{tr} \{ [\partial^\alpha \Phi^{\mu\nu}, \Phi^{\tau\beta}]_+ \partial_\tau \Phi \}
\end{aligned}$$

where the Goldstone-boson field Φ , the vector-meson field $\Phi_{\mu\nu}$, the charge matrix Q , and the mass matrix χ_0 are normalized as follows:

$$\begin{aligned}
\Phi &= \begin{pmatrix} \pi^0 + \frac{1}{\sqrt{3}} \eta & \sqrt{2} \pi^+ & \sqrt{2} K^+ \\ \sqrt{2} \pi^- & -\pi^0 + \frac{1}{\sqrt{3}} \eta & \sqrt{2} K^0 \\ \sqrt{2} K^- & \sqrt{2} \bar{K}^0 & -\frac{2}{\sqrt{3}} \eta \end{pmatrix}, \\
\Phi_{\mu\nu} &= \begin{pmatrix} \rho_{\mu\nu}^0 + \omega_{\mu\nu} & \sqrt{2} \rho_{\mu\nu}^+ & \sqrt{2} K_{\mu\nu}^+ \\ \sqrt{2} \rho_{\mu\nu}^- & -\rho_{\mu\nu}^0 + \omega_{\mu\nu} & \sqrt{2} K_{\mu\nu}^0 \\ \sqrt{2} K_{\mu\nu}^- & \sqrt{2} \bar{K}_{\mu\nu}^0 & \sqrt{2} \phi_{\mu\nu} \end{pmatrix}, \\
\chi_0 &= \begin{pmatrix} m_\pi^2 & 0 & 0 \\ 0 & m_\pi^2 & 0 \\ 0 & 0 & 2m_K^2 - m_\pi^2 \end{pmatrix}, \\
Q &= \begin{pmatrix} \frac{2}{3} & 0 & 0 \\ 0 & -\frac{1}{3} & 0 \\ 0 & 0 & -\frac{1}{3} \end{pmatrix}. \tag{2}
\end{aligned}$$

Note that we assume perfect isospin symmetry throughout this work. In (1) the photon field is denoted by A_μ and $e = 0.303$ is the electromagnetic charge. For vector mesons we use the antisymmetric tensor-field representation $\Phi_{\mu\nu} = -\Phi_{\nu\mu}$ giving rise to the resonance-saturation mechanism [21]. In principle, in the hadrogenesis conjecture also the singlet eta field is part of the ‘‘quasi-fundamental’’ hadronic degrees of freedom. It can be included in the flavor matrix of Φ in a straightforward way [20]. However, as discussed in the introduction, we do not include vector channels in our coupled-channel approach. Consequently we also do not include channels with the η' which would appear in the same energy regime. Vector mesons are important, nonetheless, as they contribute as exchange particles to the coupled channels $\gamma\gamma$ and PP . On the other hand, this is not the case for the η' . Consequently, here we have not considered the eta singlet explicitly in our Lagrangian.

Finally we shall discuss the coupling constants appearing in (1). The following set of parameters has been determined by the masses and decay properties of the vector mesons [19, 39]:

$$\begin{aligned}
f_V &= 0.140 \pm 0.014 \text{ GeV}, & h_A &\simeq 2.10, \\
h_P f_V &= 0.23 \text{ GeV}, & b_D &= 0.92, \\
f &\simeq 0.90 \text{ GeV}, & b_A &= 0.27. \tag{3}
\end{aligned}$$

The values of the other parameters g_{1-3} , g_5 and h_O have not been determined so far. Assuming that they are of natural size we will study in section 5 the impact of variations of these parameters on the photon-fusion processes and on the related decay $\eta \rightarrow \pi^0 \gamma \gamma$.

Table 1 The coupled-channel states I^G characterized by isospin I and G-parity G . The Pauli matrices σ_i act on isospin-doublet fields K, \bar{K} with for instance $K = (K^+, K^0)^t$. Note that in particular the neutral ($I_3 = 0$) two-pion state with isospin two is given by $\frac{1}{\sqrt{6}} (2\pi_p^0 \pi_q^0 - \pi_p^+ \pi_q^- - \pi_p^- \pi_q^+)$.

0 ⁺	1 ⁻
$ \begin{pmatrix} (\gamma\gamma) \\ \frac{1}{\sqrt{3}} (\pi_q \cdot \pi_p) \\ \frac{1}{2} (\bar{K}_q K_p + \bar{K}_p K_q) \\ (\eta_q \eta_p) \end{pmatrix} $	$ \begin{pmatrix} (\gamma\gamma) \\ (\pi_q \eta_p)_{I_3=0} \\ \frac{1}{2} (\bar{K}_q \boldsymbol{\sigma} K_p + \bar{K}_p \boldsymbol{\sigma} K_q)_{I_3=0} \end{pmatrix} $
2 ⁺	
$ \begin{pmatrix} (\gamma\gamma) \\ \left(\frac{1}{2} (\pi_q^i \pi_p^j + \pi_q^j \pi_p^i) - \frac{1}{3} \delta_{ij} \pi_q \cdot \pi_p \right)_{I_3=0} \end{pmatrix} $	

3 Partial-wave amplitudes

We define the transition amplitude for the process $\gamma\gamma \rightarrow PP$ as

$$\begin{aligned}
\langle P(\bar{p}) P(\bar{q}) | T | A(k_1, \lambda_1) A(k_2, \lambda_2) \rangle = & \tag{4} \\
(2\pi)^4 \delta^4(k_1 + k_2 - \bar{p} - \bar{q}) T^{\mu\nu} \epsilon_\mu(k_1, \lambda_1) \epsilon_\nu(k_2, \lambda_2) &
\end{aligned}$$

where $k_{1,2}$ and $\epsilon_{1,2}$ are the momenta and the polarization vectors of the incoming photons, respectively, and \bar{p}, \bar{q} are the momenta of the outgoing mesons.

In general, the two-body scattering problem decouples into orthogonal channels specified by isospin, G-parity, parity and strangeness quantum numbers. For the case at hand, with two photons in the initial state and two pseudoscalars in the final state, parity is always positive (see below) and strangeness is always zero. In each of the channels, finally specified by isospin I and G-parity G , there are several meson-meson states coupled to each other. In Table 1 we have specified the states which contain the most relevant meson-meson information below 1.2 GeV. Here we are neglecting multi-pion states which are only relevant for higher energies. In particular we neglect in this way also PV and VV states which on account of the resonant nature of the vector, V , states would significantly contribute to the multi-pion states.

Lorentz covariance and gauge invariance lead to a decomposition of the scattering amplitude $T^{\mu\nu}$ into

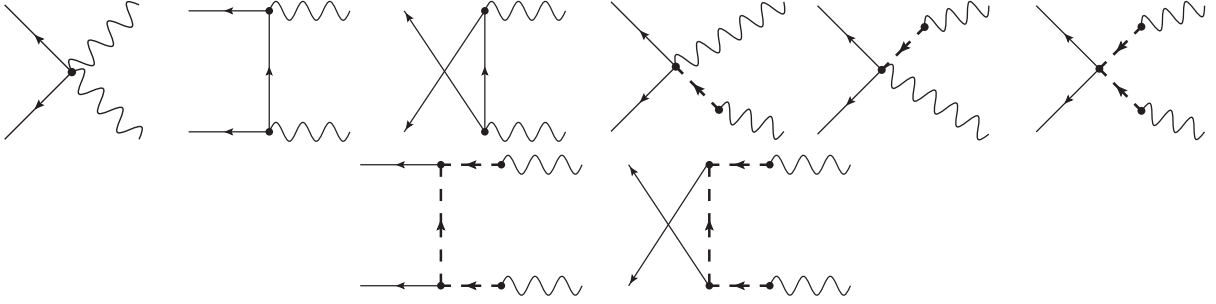


Fig. 1 Tree-level diagrams for $\gamma\gamma \rightarrow PP$ reactions with the exchange of pseudoscalar (solid line) and light vector (dashed line) mesons.

Lorentz tensors $L_i^{\mu\nu}$ and invariant amplitudes F_i ,

$$\begin{aligned} T^{\mu\nu} &= F_1(s, t, u) L_1^{\mu\nu} + F_2(s, t, u) L_2^{\mu\nu}, \\ L_1^{\mu\nu} &= k_1^\nu k_2^\mu - (k_1 \cdot k_2) g^{\mu\nu}, \\ L_2^{\mu\nu} &= (\Delta^2 (k_1 \cdot k_2) - 2(k_1 \cdot \Delta)(k_2 \cdot \Delta)) g^{\mu\nu} \\ &\quad - \Delta^2 k_1^\nu k_2^\mu - 2(k_1 \cdot k_2) \Delta^\mu \Delta^\nu \\ &\quad + 2(k_2 \cdot \Delta) k_1^\nu \Delta^\mu + 2(k_1 \cdot \Delta) k_2^\mu \Delta^\nu, \end{aligned} \quad (5)$$

where $\Delta = \bar{p} - \bar{q}$ and $T^{\mu\nu}$ satisfies the Ward identities

$$k_{1\mu} T^{\mu\nu} = k_{2\nu} T^{\mu\nu} = 0. \quad (6)$$

The motivation for choosing these particular Lorentz structures is twofold. First, the corresponding invariant amplitudes are independent and free of kinematical singularities or zeros. Second, in order to simplify further calculations we have chosen the Lorentz tensors such that the following property holds:

$$L_1^{\mu\nu} L_{2\mu\nu} = 0. \quad (7)$$

The invariant amplitudes F_1 and F_2 are analytic functions of s , t and u except for dynamical cuts. Furthermore, a $t - u$ crossing symmetry is satisfied due to the Bose statistics of the two photons.

It is useful to introduce the helicity components of the scattering amplitude and decompose each of them into their partial waves,

$$\begin{aligned} \phi_{++} &= T^{\mu\nu} \epsilon_\mu(k_1, +1) \epsilon_\nu(k_2, +1) \\ &= \sum_{\text{even } J \geq 0} (2J+1) t_{++}^{(J)} d_{00}^{(J)}(\cos \theta), \\ \phi_{+-} &= T^{\mu\nu} \epsilon_\mu(k_1, +1) \epsilon_\nu(k_2, -1) \\ &= \sum_{\text{even } J \geq 2} (2J+1) t_{+-}^{(J)} d_{20}^{(J)}(\cos \theta), \end{aligned} \quad (8)$$

where

$$\begin{aligned} \epsilon_\mu(\mathbf{k}_1, \lambda = \pm 1) &= \begin{pmatrix} 0 \\ \mp \frac{1}{\sqrt{2}} \\ -\frac{i}{\sqrt{2}} \\ 0 \end{pmatrix}, \\ \epsilon_\nu(\mathbf{k}_2 = -\mathbf{k}_1, \lambda = \pm 1) &= \begin{pmatrix} 0 \\ \pm \frac{1}{\sqrt{2}} \\ -\frac{i}{\sqrt{2}} \\ 0 \end{pmatrix}, \end{aligned}$$

and $d_{\lambda, \bar{\lambda}}^{(J)}(\cos \theta)$ are Wigner rotation functions. In (8) θ is the center-of-mass scattering angle. The axis of the colliding photons in their center-of-mass frame has been chosen to agree with the third axis of the coordinate system. Note that the partial-wave expansion involves only even $J \geq \lambda$ and positive parity $P = +$ [41]. This constraint arises from the combination of Bose symmetry of the two initial massless photons with the possible J, P quantum numbers of the two Goldstone bosons in the final state.

The invariant amplitudes $F_{1,2}$ can be expressed in terms of the helicity amplitudes ϕ_{++}, ϕ_{+-} ,

$$\begin{pmatrix} F_1 \\ F_2 \end{pmatrix} = \begin{pmatrix} -\frac{2}{s} & 0 \\ 0 & \frac{1}{2s\bar{p}_{cm}^2(x^2-1)} \end{pmatrix} \begin{pmatrix} \phi_{++} \\ \phi_{+-} \end{pmatrix} \quad (9)$$

where \bar{p}_{cm} is the final center-of-mass relative momentum and $x = \cos \theta$. For unpolarized photons the differential cross section is given by

$$\frac{d\sigma}{d\cos\theta} = \frac{\beta}{32\pi s} \frac{1}{4} (2|\phi_{++}|^2 + 2|\phi_{+-}|^2), \quad (10)$$

where $\beta = 2\bar{p}_{cm}/\sqrt{s}$. If two identical particles appear in the final state (neutral pions, for instance) one has to include an additional factor of $1/2$ in (10) or perform the integration only over $\theta \in [0, \pi/2]$.

According to (8) the partial-wave helicity amplitudes $t_{++}^{(J)}, t_{+-}^{(J)}$ can be computed in terms of the in-

variant amplitudes $F_{1,2}$ as

$$t_{++}^{(J)}(s) = -\int \frac{dx}{4} s F_1(s, x) d_{00}^{(J)}(x),$$

$$t_{+-}^{(J)}(s) = \int \frac{dx}{2} 2\bar{p}_{cm}^2 s (x^2 - 1) F_2(s, x) d_{20}^{(J)}(x), \quad (11)$$

with the help of the useful identities for the Wigner rotation functions [42]

$$d_{00}^{(J)}(x) = P_J(x),$$

$$d_{20}^{(J)}(x) = \frac{2x P_J'(x)}{\sqrt{(J-1)J(J+1)(J+2)}} - \sqrt{\frac{J(J+1)}{(J-1)(J+2)}} P_J(x). \quad (12)$$

In order to avoid kinematical singularities and zeros in the partial-wave amplitudes at threshold, we rescale (11) by a phase-space factor $(p_{cm} \bar{p}_{cm})^J$,

$$T_{++}^{(J)} = \frac{s^J}{(p_{cm} \bar{p}_{cm})^J} t_{++}^{(J)},$$

$$T_{+-}^{(J)} = \frac{s^J}{(p_{cm} \bar{p}_{cm})^J} t_{+-}^{(J)}, \quad (13)$$

and also multiply by s^J to ensure a finite limit of the phase-space matrices at large energy.

The invariant amplitudes (5) computed from the chiral Lagrangian (1) read

$$F_1 = \frac{e^2 C_{SG}}{2s} - \sum_{x \in [8]} \frac{e^2 (m_x^4 - tu) C_0^{(x)}}{2s^2 (t - m_x^2)}$$

$$+ \sum_{x \in [9]} \left(\frac{e^2 f_V^2}{8 f^2} \frac{C_1^{(x)}}{m_x^2} - \frac{e^2 f_V^2 h_P}{8 f^2} \frac{C_{h_P}^{(x)}}{m_x^2} \right)$$

$$+ \sum_{x, y \in [9]} \frac{e^2 f_V^2}{32 f^2} \frac{1}{m_x^2 m_y^2} \left((g_1 C_{g_1}^{(x, y)} + g_2 C_{g_2}^{(x, y)} + g_3 C_{g_3}^{(x, y)} + g_5 C_{g_5}^{(x, y)}) (s - \bar{m}_1^2 - \bar{m}_2^2) - \frac{1}{2} b_D C_{b_D}^{(x, y)} \right)$$

$$+ \sum_{x, y, z \in [9]} \frac{e^2 f_V^2}{16 f^2} \frac{1}{m_x^2 m_y^2} \left(\frac{1}{16} \frac{t^2}{m_z^2} h_O^2 C_{h_O}^{(x, y, z)} - \frac{1}{16} \frac{t^2}{t - m_z^2} h_A^2 C_{h_A}^{(x, y, z)} + \frac{t - 2m_z^2}{m_z^2} \frac{1}{t - m_z^2} b_A^2 C_{b_A}^{(x, y, z)} + \frac{1}{2} \frac{t}{t - m_z^2} b_A h_A C_{b_A h_A}^{(x, y, z)} + \frac{1}{2} \frac{t}{m_z^2} b_A h_O C_{b_A h_O}^{(x, y, z)} \right)$$

$$+ (t \leftrightarrow u),$$

$$F_2 = - \sum_{x \in [8]} \frac{e^2 C_0^{(x)}}{8s(t - m_x^2)}$$

$$- \sum_{x, y \in [9]} \frac{e^2 f_V^2}{64 f^2} \frac{1}{m_x^2 m_y^2} \left(g_3 C_{g_3}^{(x, y)} + g_5 C_{g_5}^{(x, y)} \right)$$

$$+ \sum_{x, y, z \in [9]} \frac{e^2 f_V^2}{64 f^2} \frac{1}{m_x^2 m_y^2} \left(\frac{1}{16} \frac{t}{m_z^2} h_O^2 C_{h_O}^{(x, y, z)} + \frac{1}{16} \frac{t}{t - m_z^2} h_A^2 C_{h_A}^{(x, y, z)} + \frac{1}{m_z^2} \frac{1}{t - m_z^2} b_A^2 C_{b_A}^{(x, y, z)} - \frac{1}{2} \frac{1}{t - m_z^2} b_A h_A C_{b_A h_A}^{(x, y, z)} + \frac{1}{2} \frac{1}{m_z^2} b_A h_O C_{b_A h_O}^{(x, y, z)} \right)$$

$$+ (t \leftrightarrow u), \quad (14)$$

where the sum runs over the octet of Goldstone bosons ([8]) or the vector-meson nonet ([9]) and $m_{x,y,z}$ denotes their respective masses. The coefficients C_{\dots} are presented in Tables 3, 4, 5, and 6 with respect to the coupled-channel states of Table 1. In Fig. 1 the set of tree-level diagrams that gives nonzero contributions is depicted. Note that for the isospin states which contain identical particles (e.g. $|\pi\pi\rangle$, $|\eta\eta\rangle$, ...) we use a convention where the unitarity condition for identical and non-identical two-particle states are the same.

The conventions of Table 1 imply the following relations between scattering amplitudes in isospin and particle bases,

$$T_{\gamma\gamma \rightarrow \pi^+\pi^-} = 2 \left(\frac{1}{\sqrt{3}} T_{\gamma\gamma \rightarrow \pi\pi}^{I=0} - \frac{1}{\sqrt{6}} T_{\gamma\gamma \rightarrow \pi\pi}^{I=2} \right),$$

$$T_{\gamma\gamma \rightarrow \pi^0\pi^0} = 2 \left(\frac{1}{\sqrt{3}} T_{\gamma\gamma \rightarrow \pi\pi}^{I=0} + \sqrt{\frac{2}{3}} T_{\gamma\gamma \rightarrow \pi\pi}^{I=2} \right),$$

$$T_{\gamma\gamma \rightarrow \pi^0\eta} = \sqrt{2} T_{\gamma\gamma \rightarrow \pi\eta}^{I=1}, \quad T_{\gamma\gamma \rightarrow \eta\eta} = 2 T_{\gamma\gamma \rightarrow \eta\eta}^{I=0},$$

$$T_{\gamma\gamma \rightarrow K^+K^-} = T_{\gamma\gamma \rightarrow K\bar{K}}^{I=0} + T_{\gamma\gamma \rightarrow K\bar{K}}^{I=1},$$

$$T_{\gamma\gamma \rightarrow K^0\bar{K}^0} = T_{\gamma\gamma \rightarrow K\bar{K}}^{I=0} - T_{\gamma\gamma \rightarrow K\bar{K}}^{I=1}, \quad (15)$$

where the factor 2 reflects our normalization for two-body states with identical particles. Note that in [12] meson-meson interactions were studied only for S- and P-waves. The result for the D-wave amplitude can easily be obtained from Eq. (4) and Eq. (5) of [12].

The partial-wave amplitudes obtained from (13, 11) and (14) at tree-level will serve as an input for the non-perturbative coupled-channel calculations to which we turn next.

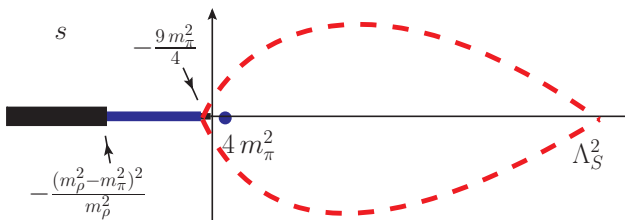


Fig. 2 Locations of left-hand cuts of the $\gamma\gamma \rightarrow \pi\pi$ partial-wave amplitude in the complex s -plane. The branch point of the ρ -meson exchange is located at $\Lambda_0^2 = -(m_\rho^2 - m_\pi^2)^2/m_\rho^2$, while one- and two-pion exchange cuts start at $\Lambda_0^2 = 0$, $-9m_\pi^2/4$, respectively. The dashed line identifies the convergence region of the conformal expansion (20).

4 Coupled-channel dynamics

The partial-wave reaction amplitudes satisfy the dispersion-integral representation,

$$T_{ab}^J(s) = U_{ab}^J(s) + \sum_{c,d} \int_{\mu_{\text{thr}}^2}^{\infty} \frac{d\bar{s}}{\pi} \frac{s - \mu_M^2}{\bar{s} - \mu_M^2} \frac{T_{ac}^J(\bar{s}) \rho_{cd}^J(\bar{s}) T_{db}^{J*}(\bar{s})}{\bar{s} - s - i\epsilon}, \quad (16)$$

where the phase-space matrix $\rho_{cd}^J(s)$ is diagonal in c and d . In (16) the coupled-channel indices a and b run over the various channel $\gamma\gamma$, $\pi\pi$, $K\bar{K}$ etc. The unitarity condition implies that the discontinuity of the generalized potential

$$\Delta U_{ab}^J(s) = \frac{1}{2i} (U_{ab}^J(s + i\epsilon) - U_{ab}^J(s - i\epsilon)) = 0 \quad \text{for} \quad s \geq \mu_{\text{thres}}^2, \quad (17)$$

vanishes for energies larger than the s -channel threshold. This is nothing but the condition that $U_{ab}^J(s)$ has left-hand cuts only.

In our normalization the hadronic part of the phase-space matrix

$$\rho^J(s) = \frac{1}{8\pi} \left(\frac{p_{cm}}{\sqrt{s}} \right)^{2J+1} \Theta(s - \mu_{\text{thr}}^2), \quad (18)$$

approaches a finite value in the high-energy limit. Intermediate states with two photons are neglected in this work. Numerically they are largely suppressed being proportional to e^4 at least. Therefore the two-dimensional phase-space matrix for the two-photon states need not to be specified here.

Our approach satisfies the electromagnetic gauge-invariance constraint. This follows from the on-shell condition for the generalized potential, for which we will construct a systematic approximation in the following. The on-shell reaction amplitude will then be derived in application of (16). Owing to the matching scale μ_M in (16) the non-perturbative coupled-channel calculation and the results from a perturbative application of the

Table 2 The positions of the closest left-hand branch points of $U_{\text{outside}}(s)$ for $\gamma\gamma \rightarrow PP$ that are determined by the t - and u -channel exchange processes. The numbers in the column “ch = ab” correspond to the out-states (a) and in-states (b) of Table 1.

I^G	ch.	μ_E^2	Λ_0^2	Description
0 ⁺	21	m_π^2	$-\frac{9m_\pi^2}{4}$	t, u -ch (2π)
	31	m_K^2	$-\frac{m_\pi^2(m_\pi + 2m_K)^2}{(m_\pi + m_K)^2}$	t, u -ch (πK)
	41	m_η^2	0	t, u -ch (2π)
1 ⁻	21	$\frac{(m_\pi + m_\eta)^2}{4}$	$\frac{3}{4}(m_\eta^2 - 4m_\pi^2)$	t, u -ch (2π)
	31	m_K^2	$-\frac{m_\pi^2(m_\pi + 2m_K)^2}{(m_\pi + m_K)^2}$	t, u -ch (πK)
2 ⁺	21	m_π^2	$-\frac{9m_\pi^2}{4}$	t, u -ch (2π)

chiral Lagrangian smoothly connect at $s = \mu_M^2$. This is discussed in detail in [10] and [12]. Here we identify μ_M with the smallest two-body hadronic threshold value and thereby assume the applicability of χ PT at $s = \mu_M^2$.

Following [10] the generalized potential $U_{ab}^J(s)$ can be extrapolated to higher energies in a controlled manner by applying conformal mapping techniques. In a first step the generalized potential is split into two contributions ²

$$U(s) = U_{\text{inside}}(s) + U_{\text{outside}}(s), \quad (19)$$

where $U_{\text{inside}}(s)$ contains the contributions from close-by left-hand cuts and $U_{\text{outside}}(s)$ the contributions from far-distant left-hand cuts. While the former can be explicitly calculated from the chiral Lagrangian in a perturbative application, the latter reflect short distance physics that need to be parameterized systematically and efficiently. For the specific example reaction $\gamma\gamma \rightarrow \pi\pi$ the separation of ‘inside’ and ‘outside’ is implied by the dashed line in Fig. 2.

The outside potential is expanded in powers of a conformal variable $\xi(s)$ constructed such as to ensure convergence for any value of s inside the area bounded by the dashed line of Fig. 2,

$$U_{\text{outside}}(s) = \sum_{k=0}^n c_k \xi^k(s) \quad \text{for} \quad s < \Lambda_S^2, \quad (20)$$

where the coefficients c_k are uniquely determined by the first k derivatives of $U_{\text{outside}}(s)$ at the expansion point $s = \mu_E^2$. We identify this expansion point with the mean

²In the following we do not display any more the angular-momentum superscript J explicitly. Where not needed we also do not display the channel index ab .

of the initial and the final threshold. Following [12] the function $\xi(s)$ takes the form

$$\xi(s) = \frac{a(\Lambda_s^2 - s)^2 - 1}{(a - 2b)(\Lambda_s^2 - s)^2 + 1}, \quad (21)$$

$$a = \frac{1}{(\Lambda_s^2 - \mu_E^2)^2}, \quad b = \frac{1}{(\Lambda_s^2 - \Lambda_0^2)^2},$$

where the parameter Λ_0 is determined by the positions of the closest left-hand branch point of the structures which enter U_{outside} . The quantities μ_E (expansion point for outside potential) are collected in Table 2 for the isospin states of Table 1. Finally, Λ_s is the upper limit of the convergence region, see Fig. 2.

To be specific, the 'inside' part of the potential receives contributions from the one-pion (kaon) exchange processes only. We evaluate the contributions from the cuts starting from

$$\begin{aligned} -\frac{9m_\pi^2}{4} < s < 0 & \quad \text{for } \gamma\gamma \rightarrow \pi\pi, \\ -m_\pi^2 \frac{(m_\pi + 2m_K)^2}{(m_\pi + m_K)^2} < s < 0 & \quad \text{for } \gamma\gamma \rightarrow K\bar{K}, \end{aligned} \quad (22)$$

following the procedure outlined in Appendix B of [10]. According to Table 3 there are no more cases to be considered. The coefficients c_k in the outside part of the potential are computed by evaluating the first n derivatives of the partial-wave amplitudes as determined via (11, 12) by the tree-level result (14).

Via (19) we obtain an approximated generalized potential for energies $\Lambda_0^2 < s < \Lambda_s^2$. While the inside part of the potential is defined for $s > \Lambda_s^2$ also, the outside part is undefined for $s > \Lambda_s^2$ by (20). We may simply cut off the integral in (16) at $\bar{s} = \Lambda_s^2$. However, it is advantageous not to do so, since that would induce rapid variations of the amplitudes close to and below $s = \Lambda_s$. While the precise form of the generalized potential at $s > \Lambda_s^2$ should not influence the reaction amplitudes in the target region, where we have a controlled expansion, it is useful to minimize its residual influence on the target region. This is the case if the outside potential is smoothly extended for $s > \Lambda_s^2$ by a constant (see [10, 11, 12, 13]). We note that due to the particular form of the conformal map (21), the generalized potential and its derivative are continuous at $s = \Lambda_s^2$.

Following [12, 43], we choose in the following $n = 3$ in (20) and $\Lambda_s = 1.6 \text{ GeV}$. We have varied Λ_s in the range 1.4 GeV to 1.8 GeV. The impact of this variation on the results is small [43].

A crucial observation behind our summation scheme is the fact that the computation of the partial-wave scattering amplitude from (16) at energies larger than threshold also requires only the knowledge of the generalized potential at energies larger than threshold. More generally, depending on where we want to compute the

Table 3 The coefficients C_{SG} , $C_0^{(x)}$ and $C_1^{(x)} = 2C_{\mu_P}^{(x)}$ of the invariant amplitudes (14) with respect to the coupled-channel states I^G of Table 1. The numbers in the column "ch = ab" correspond to the out-states (a) and in-states (b) of Table 1.

I^G	0 ⁺	0 ⁺	1 ⁻	2 ⁺
ch.	21	31	31	21
C_{SG}	$-\frac{8}{\sqrt{3}}$	-4	-4	$4\sqrt{\frac{2}{3}}$
$C_0^{(\pi)}$	$-\frac{8}{\sqrt{3}}$	0	0	$4\sqrt{\frac{2}{3}}$
$C_0^{(K)}$	0	-4	-4	0
$C_1^{(\rho)}$	$\frac{16}{\sqrt{3}}$	4	4	$-8\sqrt{\frac{2}{3}}$
$C_1^{(\omega)}$	0	$\frac{4}{3}$	$\frac{4}{3}$	0
$C_1^{(\phi)}$	0	$\frac{8}{3}$	$\frac{8}{3}$	0

partial-wave scattering amplitudes, it suffices to construct a controlled approximation of the generalized potential in a specific region of the complex plane only. This is always achieved with (19, 20) and the desired solution of (16) can be found by the N/D ansatz [44]

$$T_{ab}(s) = \sum_c D_{ac}^{-1}(s) N_{cb}(s), \quad (23)$$

where $D_{ab}(s)$ contains only the right-hand s-channel unitarity cuts,

$$D_{ab}(s) = \delta_{ab} - \sum_c \int_{\mu_{\text{thr}}^2}^{\infty} \frac{d\bar{s}}{\pi} \frac{s - \mu_M^2}{\bar{s} - \mu_M^2} \frac{N_{ac}(\bar{s}) \rho_{cb}(\bar{s})}{\bar{s} - s - i\epsilon}, \quad (24)$$

and the matrix $N_{ab}(s)$ contains left-hand cuts only,

$$\begin{aligned} N_{ab}(s) &= U_{ab}(s) \\ &+ \sum_{c,d} \int_{\mu_{\text{thr}}^2}^{\infty} \frac{d\bar{s}}{\pi} \frac{s - \mu_M^2}{\bar{s} - \mu_M^2} N_{ac}(\bar{s}) \rho_{cd}(\bar{s}) \frac{U_{db}(\bar{s}) - U_{db}(s)}{\bar{s} - s}. \end{aligned} \quad (25)$$

The system (25) with the input (19), (20) can be solved numerically by the method of matrix inversion.

5 Numerical results

In this section we present our results for the cross sections³ of the reactions $\gamma\gamma \rightarrow \pi^0\pi^0, \pi^+\pi^-, K^0\bar{K}^0, K^+K^-, \eta\eta$ and $\pi^0\eta$, evaluated with the $J = 0, 2$ partial-wave amplitudes. We have checked that the contributions from the higher partial waves are negligible in the energy range $\sqrt{s} < 1.2 \text{ GeV}$.

³Usually the experimental results are limited to a range of $|x| \leq Z$ with $x = \cos\theta$. In this case the cross section is given by $\sigma = 2 \int_0^Z \frac{d\sigma}{dx} dx$.

Table 4 The coefficients $C_{b_A h_A}^{(x,y,z)} = C_{b_A h_O}^{(x,y,z)}$. See the caption of Table 3 for more details.

		$C_{b_A h_A}^{(x,y,z)}$						
I^G	ch.	(ρ, ρ, ρ)	(ρ, ρ, ω)	(ρ, ρ, K^*)	(ρ, ω, ρ) (ω, ρ, ω)	(ρ, ω, K^*) (ω, ρ, K^*)	(ρ, ϕ, K^*) (ϕ, ρ, K^*)	
0^+	21	0	$\frac{32 m_\pi^2}{\sqrt{3}}$	0	0	0	0	
	31	0	0	$32 m_K^2$	0	0	0	
	41	$\frac{32 m_\pi^2}{3}$	0	0	0	0	0	
1^-	21	0	0	0	$\frac{32}{3} \sqrt{\frac{2}{3}} m_\pi^2$	0	0	
	31	0	0	0	0	$\frac{16 m_K^2}{3}$	$-\frac{32 m_K^2}{3}$	
2^+	21	0	$32 \sqrt{\frac{2}{3}} m_\pi^2$	0	0	0	0	
		(ω, ω, ρ)	(ω, ω, ω)	(ω, ω, K^*)	(ω, ϕ, K^*) (ϕ, ω, K^*)	(ϕ, ϕ, K^*)	(ϕ, ϕ, ϕ)	
0^+	21	$\frac{32 m_\pi^2}{3\sqrt{3}}$	0	0	0	0	0	
	31	0	0	$\frac{16 m_K^2}{9}$	$-\frac{32 m_K^2}{9}$	$\frac{64 m_K^2}{9}$	0	
	41	0	$\frac{32 m_\pi^2}{27}$	0	0	0	$\frac{32}{27} (16 m_K^2 - 8 m_\pi^2)$	

We use the set of parameters given in (3) for all the numerical results. However, the remaining five parameters g_1, g_2, g_3, g_5 and h_O have to be determined. Our strategy is to use the empirical data on the reactions $\gamma\gamma \rightarrow \pi^0\pi^0, \pi^+\pi^-$ and $\pi^0\eta$ and in addition the differential and integrated data for the decay $\eta \rightarrow \pi^0\gamma\gamma$. The results for the cross sections of the reactions $\gamma\gamma \rightarrow K^0\bar{K}^0, K^+K^-$ and $\eta\eta$ are then pure predictions.

On account of crossing symmetry, the decay amplitude for $\eta \rightarrow \pi^0\gamma\gamma$ can be easily obtained from $\gamma\gamma \rightarrow \pi^0\eta$ by considering π^0 and photons as outgoing particles. To get the decay amplitude it is enough to replace

$$\begin{aligned} s &= (k_1 + k_2)^2 \rightarrow (\bar{k}_1 + \bar{k}_2)^2 = M_{\gamma\gamma}^2, \\ t &= (p - k_1)^2 \rightarrow (p_\pi + \bar{k}_1)^2 = M_{\gamma_1\pi}^2, \\ u &= (p - k_2)^2 \rightarrow (p_\pi + \bar{k}_2)^2 = M_{\gamma_2\pi}^2, \end{aligned} \quad (26)$$

in the invariant amplitudes (14). The differential decay rate is given by [45]

$$d\Gamma = \frac{1}{(2\pi)^3} \frac{1}{32 m_\eta^3} \sum_{pol} |T_{\eta \rightarrow \pi^0\gamma\gamma}|^2 dM_{\gamma\gamma}^2 dM_{\gamma_2\pi}^2. \quad (27)$$

For the integrated partial decay width one has to include the degeneracy factor of 1/2 to account for the fact that one has two indistinguishable photons in the final state. To obtain the *decay* amplitude we use directly the tree-level result (14). Since we are here in the low-energy decay region, we assume that coupled-channel effects are less important. For the *reaction* amplitudes we use, of course, the full rescattering formalism outlined in the previous section.

In a first step we use the reaction data of $\gamma\gamma \rightarrow \pi^0\pi^0, \pi^+\pi^-$ and $\pi^0\eta$ to correlate the five free parameters. Having matched the data with the coupled-channel calculations leads to the following relations:

$$\begin{aligned} g_1 &= 0.900 - 0.200 g_3 + 0.038 h_O^2 + 0.128 h_O, \\ g_2 &= -1.50 - 0.27 g_3 + 0.25 g_5. \end{aligned} \quad (28)$$

This leaves us with three free parameters. If they are varied within the range $g_3, g_5, h_O \in [-5, 5]$ one obtains the cross sections depicted in Fig. 3. A detailed discussion of the cross sections will be given below. To get a feeling for the influence of the five parameters we also provide the cross sections for the case where all these five parameters are put to zero, see the dashed lines in Fig. 3. Obviously, one would significantly underestimate the data in both neutral channels $\pi^0\pi^0$ and $\pi^0\eta$ without the parameters g_i and h_O . Note, however, that the qualitative structure does not depend so much on these parameters.

We continue with a determination of the remaining parameters using the existing data on $\eta \rightarrow \pi^0\gamma\gamma$ decay. The present experimental status for $\eta \rightarrow \pi^0\gamma\gamma$ decay is the following: The Particle Data Group [45] gives the branching ratio $\Gamma_{\eta \rightarrow \pi^0\gamma\gamma}/\Gamma_\eta = (2.7 \pm 0.5) \cdot 10^{-4}$ and the full width $\Gamma_\eta = (1.30 \pm 0.07)$ keV. This results in a partial decay width of $\Gamma_{\eta \rightarrow \pi^0\gamma\gamma} \approx (0.35 \pm 0.09)$ eV. Theoretical studies have been performed in [47, 48, 49].

For the decay $\eta \rightarrow \pi^0\gamma\gamma$ three of the yet undetermined parameters contribute, namely g_1, g_3 and h_O . Using the relation (28) for g_1 , we adjust g_3 and h_O to

Table 5 The coefficients $C_{b_A}^{(x,y,z)}$ and $C_{h_A}^{(x,y,z)} = C_{h_O}^{(x,y,z)}$. See the caption of Table 3 for more details.

		$C_{b_A}^{(x,y,z)}$					
I^G	ch.	(ρ, ρ, ρ)	(ρ, ρ, ω)	(ρ, ρ, K^*)	(ρ, ω, ρ) (ω, ρ, ω)	(ρ, ω, K^*) (ω, ρ, K^*)	(ρ, ϕ, K^*) (ϕ, ρ, K^*)
0 ⁺	21	0	$\frac{64 m_\pi^4}{\sqrt{3}}$	0	0	0	0
	31	0	0	$32 m_K^4$	0	0	0
	41	$\frac{64 m_\pi^4}{3}$	0	0	0	0	0
1 ⁻	21	0	0	0	$\frac{64}{3} \sqrt{\frac{2}{3}} m_\pi^4$	0	0
	31	0	0	0	0	$\frac{32 m_K^4}{3}$	$-\frac{64 m_K^4}{3}$
2 ⁺	21	0	$64 \sqrt{\frac{2}{3}} m_\pi^4$	0	0	0	0
		(ω, ω, ρ)	(ω, ω, ω)	(ω, ω, K^*)	(ω, ϕ, K^*) (ϕ, ω, K^*)	(ϕ, ϕ, K^*)	(ϕ, ϕ, ϕ)
0 ⁺	21	$\frac{64 m_\pi^4}{3\sqrt{3}}$	0	0	0	0	0
	31	0	0	$\frac{32 m_K^4}{9}$	$-\frac{64 m_K^4}{9}$	$\frac{128 m_K^4}{9}$	0
	41	0	$\frac{64 m_\pi^4}{27}$	0	0	0	$\frac{64}{27} (32 m_K^4 - 32 m_\pi^2 m_K^2 + 8 m_\pi^4)$
		$C_{h_A}^{(x,y,z)}$					
I^G	ch.	(ρ, ρ, ρ)	(ρ, ρ, ω)	(ρ, ρ, K^*)	(ρ, ω, ρ) (ω, ρ, ω)	(ρ, ω, K^*) (ω, ρ, K^*)	(ρ, ϕ, K^*) (ϕ, ρ, K^*)
0 ⁺	21	0	$\frac{16}{\sqrt{3}}$	0	0	0	0
	31	0	0	8	0	0	0
	41	$\frac{16}{3}$	0	0	0	0	0
1 ⁻	21	0	0	0	$\frac{16}{3} \sqrt{\frac{2}{3}}$	0	0
	31	0	0	0	0	$\frac{8}{3}$	$-\frac{16}{3}$
2 ⁺	21	0	$16 \sqrt{\frac{2}{3}}$	0	0	0	0
		(ω, ω, ρ)	(ω, ω, ω)	(ω, ω, K^*)	(ω, ϕ, K^*) (ϕ, ω, K^*)	(ϕ, ϕ, K^*)	(ϕ, ϕ, ϕ)
0 ⁺	21	$\frac{16}{3\sqrt{3}}$	0	0	0	0	0
	31	0	0	$\frac{8}{9}$	$-\frac{16}{9}$	$\frac{32}{9}$	0
	41	0	$\frac{16}{27}$	0	0	0	$\frac{128}{27}$

the partial decay width and to the two-photon invariant-mass distribution depicted in Fig. 4. In this way we find

$$g_3 = -4.88, \quad h_O = 3.27 \quad (29)$$

which implies $g_1 = 2.70$ and $g_2 = -0.18 + 0.25 g_5$. The fit yields

$$\Gamma_{\eta \rightarrow \pi^0 \gamma \gamma} = 0.310 \text{ eV} \quad (30)$$

for the integrated partial decay width, in good agreement with the experimental value.

We have determined four of our five free parameters. In the following we will show results where the remaining free parameter g_5 is varied in the range $g_5 \in [-5, 5]$.

Note that the achieved determination of the parameters is also crucial for future investigations. Originally all these parameters concern interactions between two vector mesons and an odd (h_O) or even (g_i , $i = 1, 2, 3, 5$) number of Goldstone bosons. In the future it is planned to explore also the importance of vector-meson channels for the coupled-channel problems (cf. the corresponding discussion in the introduction and [24]). There the coupling constants h_O and g_i enter directly and mediate, e.g., the transition from two vector to two pseudoscalar mesons. For the following reason these coupling constants are also important for our case at hand, in spite

Table 6 The coefficients $C_{g_1}^{(x,y)}$, $C_{g_2}^{(x,y)}$, $C_{g_3}^{(x,y)}$, $C_{g_5}^{(x,y)}$ and $C_{b_D}^{(x,y)}$. See the caption of Table 3 for more details.

I^G	ch.	(ρ, ρ)	(ρ, ω) (ω, ρ)	(ρ, ϕ) (ϕ, ρ)	(ω, ω)	(ω, ϕ) (ϕ, ω)	(ϕ, ϕ)
$C_{g_1}^{(x,y)}$							
0^+	21	$\frac{16}{\sqrt{3}}$	0	0	$\frac{16}{3\sqrt{3}}$	0	0
	31	8	0	0	$\frac{8}{9}$	$-\frac{16}{9}$	$\frac{32}{9}$
	41	$16/3$	0	0	$\frac{16}{27}$	0	$\frac{128}{27}$
1^-	21	0	$\frac{16}{3}\sqrt{\frac{2}{3}}$	0	0	0	0
	31	0	$\frac{8}{3}$	$-\frac{16}{3}$	0	0	0
2^+	21	$16\sqrt{\frac{2}{3}}$	0	0	0	0	0
$C_{g_2}^{(x,y)}$							
0^+	21	$\frac{32}{\sqrt{3}}$	0	0	0	0	0
	31	8	0	0	$\frac{8}{9}$	$\frac{16}{9}$	$\frac{32}{9}$
1^-	21	0	$\frac{8}{3}$	$\frac{16}{3}$	0	0	0
2^+	21	$-16\sqrt{\frac{2}{3}}$	0	0	0	0	0
$C_{g_3}^{(x,y)}$							
0^+	21	$4\sqrt{3}$	0	0	$\frac{4}{3\sqrt{3}}$	0	0
	31	4	0	0	$\frac{4}{9}$	0	$\frac{16}{9}$
	41	$\frac{4}{3}$	0	0	$\frac{4}{27}$	0	$\frac{32}{27}$
1^-	21	0	$\frac{4}{3}\sqrt{\frac{2}{3}}$	0	0	0	0
	31	0	$\frac{4}{3}$	0	0	0	0
$C_{g_5}^{(x,y)}$							
0^+	21	$-\frac{8}{\sqrt{3}}$	0	0	0	0	0
	31	-2	0	0	$-\frac{2}{9}$	$-\frac{4}{9}$	$-\frac{8}{9}$
1^-	31	0	$-\frac{2}{3}$	$-\frac{4}{3}$	0	0	0
2^+	21	$4\sqrt{\frac{2}{3}}$	0	0	0	0	0
$C_{b_D}^{(x,y)}$							
0^+	21	$32\sqrt{3} m_\pi^2$	0	0	$\frac{32}{3\sqrt{3}} m_\pi^2$	0	0
	31	$32 m_K^2$	0	0	$\frac{32}{9} m_K^2$	0	$\frac{128}{9} m_K^2$
	41	$\frac{32}{3} m_\pi^2$	0	0	$\frac{32}{27} m_\pi^2$	0	$\frac{32}{27} (16 m_K^2 - 8 m_\pi^2)$
1^-	21	0	$\frac{32}{3}\sqrt{\frac{2}{3}} m_\pi^2$	0	0	0	0
	31	0	$\frac{32}{3} m_K^2$	0	0	0	0

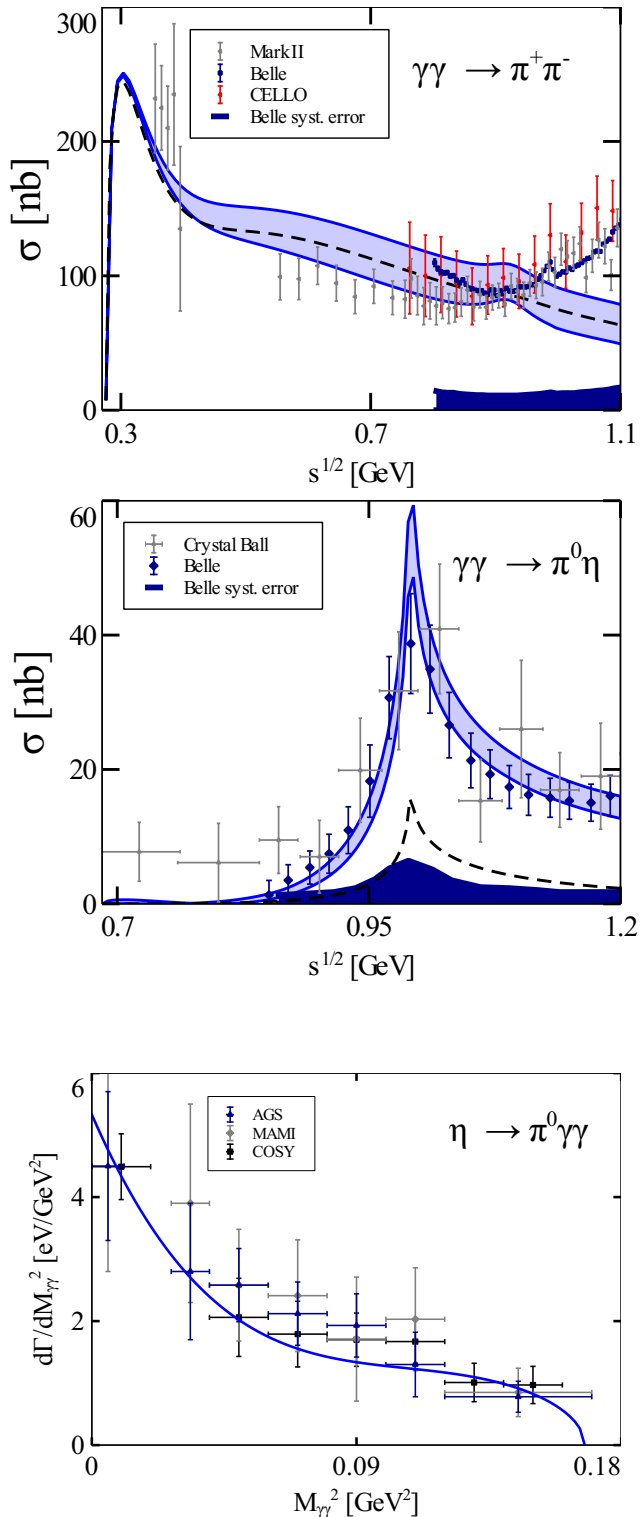


Fig. 4 The single-differential invariant-mass distribution of the decay $\eta \rightarrow \pi^0 \gamma \gamma$. Parameters are chosen according to (28), (29). Note that the parameters g_2 and g_5 do not contribute to this decay. The data are taken from [36, 37, 46].

of the fact that we do not consider the vector-meson channels: The neutral vector mesons couple directly to photons; see also Fig. 1. Therefore, the coupling con-

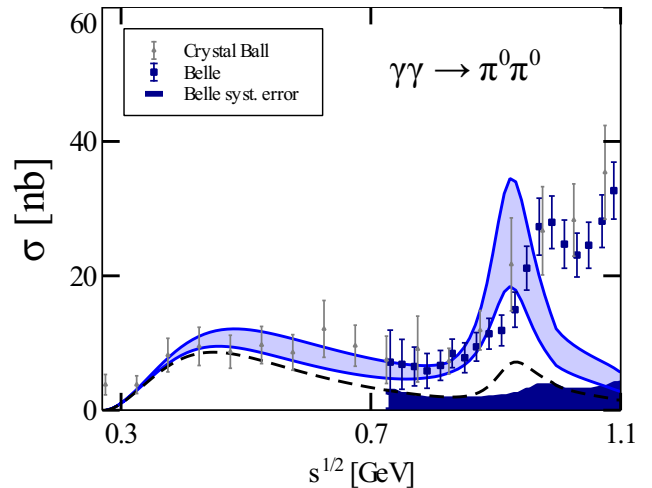


Fig. 3 Total cross sections for $\gamma\gamma \rightarrow \pi^+\pi^-$ with $|\cos\theta| < 0.6$ (top left), $\gamma\gamma \rightarrow \pi^0\pi^0$ with $|\cos\theta| < 0.8$ (top right) and $\gamma\gamma \rightarrow \pi^0\eta$ with $|\cos\theta| < 0.9$ (bottom). A variation of parameters $g_3, g_5, h_O \in [-5, 5]$ using (28) is reflected by the various bands. Setting $g_i = 0 = h_O$ yields the dashed lines. The data are taken from [27, 32, 25, 26, 33, 28, 34].

stants h_O and g_i enter also the transition amplitudes from two photons to two pseudoscalars. In turn, data on such interactions between hadrons and electromagnetism can be used to constrain purely hadronic coupling constants. This resembles our determination of h_A from the decay $\omega \rightarrow \gamma\pi^0$ in [19]. Note, however, that in our formalism this line of reasoning does not lead automatically to strict vector-meson dominance, but rather to an improved version thereof [40, 20].

We now turn to a detailed discussion of the various two-meson channels populated by photon fusion. The first highlight is the $\pi^0\eta$ channel depicted in Fig. 5. Here our formalism shows a dynamically generated scalar-isovector resonance which is in full quantitative agreement with the experimental data; see also [50, 23, 51] where similar findings have been reported. In our approach we find that this $a_0(980)$ resonance coincides with the two-kaon threshold and emerges from rescattering and coupled-channel effects between $\pi^0\eta$ and $K\bar{K}$. We contrast our full coupled-channel result with a pure tree-level calculation based on (14). The

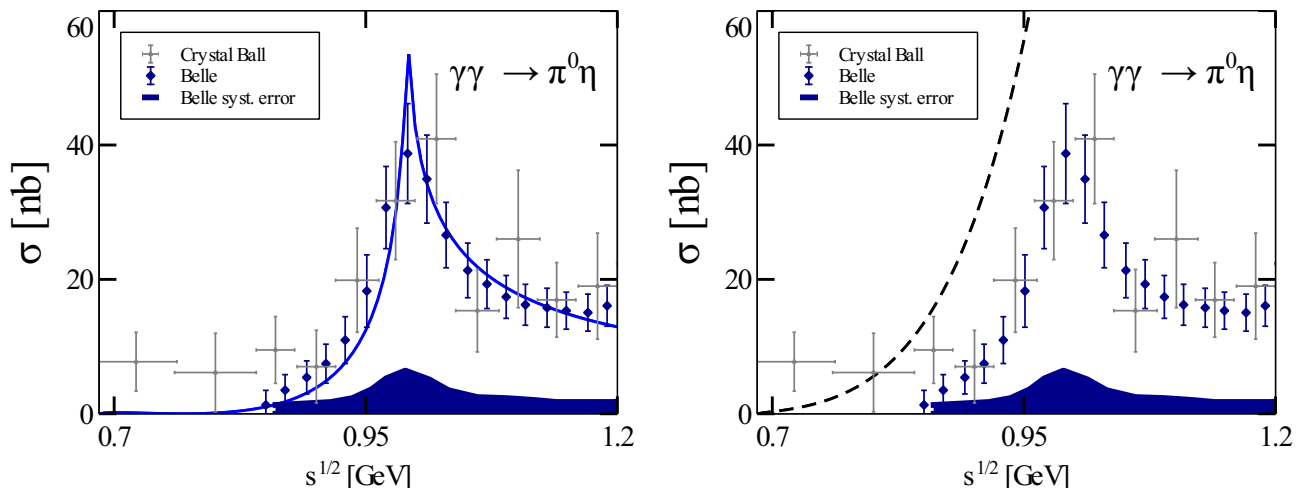


Fig. 5 Cross section for the reaction $\gamma\gamma \rightarrow \pi^0\eta$ using (28), (29) together with $g_5 \in [-5, 5]$. The full result is shown on the left and the tree-level result on the right. The tree-level result does not depend on g_5 . Also the dependence of the full result on g_5 is very weak. It is caused by the cross-channel effect $\gamma\gamma \rightarrow K\bar{K} \rightarrow \pi^0\eta$. See the figure caption of Fig. 3 for more details.

latter is also depicted in Fig. 5 and, of course, does not show a resonance shape, in obvious disagreement with the experimental data. We stress again that according to the hadrogenesis conjecture [14, 15, 16, 17, 18, 19, 20] the low-lying scalar resonances are supposed to be generated dynamically. An incarnation of this proposition is seen in Fig. 5. We recall from our previous discussion about Fig. 3 that the location of the resonance does not depend on the choice of the coupling constants g_i and h_O . Only the height of the curve is sensitive to these parameters. This provides confidence in the robustness of our interpretation of the lowest-lying scalar-isovector resonance.

The cross sections for the two-pion channels are depicted in Fig. 6. Obviously both channels $\pi^+\pi^-$ and $\pi^0\pi^0$ are well described up to energies of about $\sqrt{s} \approx 0.9$ GeV. Then our calculations show a distinct peak, most pronounced in the neutral channel. After this peak our theory curves decrease while the data continue to rise. Two issues need to be disentangled here, namely the location of the $f_0(980)$ in the S-wave and the rise towards the tensor mesons in the D-wave. To do this we compare our results also to the partial-wave analysis of [1] as shown in Fig. 7. For the D-waves (bottom panels) we observe reasonable agreement up to the point in energy where the peak from the isoscalar tensor meson starts out. As already stressed in the introduction we expect that in the spirit of the hadrogenesis conjecture this peak will be generated by vector-vector channels. But since this is beyond the present work we cannot expect to obtain a reasonable description of the D-wave beyond about 0.9 GeV. Below this energy the agreement is very satisfying. Turning to the S-wave we observe also good agreement for isospin $I = 2$ (top right panel in Fig.

7). For the isoscalar channel (top left) some disagreement with the results of [1] is observed. Most notably our peak for the $f_0(980)$ is slightly shifted to lower energies, i.e. this dynamically generated scalar-isoscalar state is somewhat overbound in our approach. This has already been observed in [12]. Whether this is due to higher-order effects in the scattering kernel or due to missing vector-vector channels remains to be seen.

For the energy range below 0.9 GeV we deduce from Fig. 6 that we have obtained an overall good description of the reaction data. This is completely in line with the complementary information contained in the pion phase shifts as addressed in [12]. In Fig. 8 we compare our calculations to the results from chiral perturbation theory (χ PT)[8, 9, 7, 6]. We observe satisfying agreement. Note that even without vector mesons our calculations contain multi-loop diagrams by the achieved resummation in the s -channel. On the other hand, our calculation does not contain all one-loop diagrams in the t - and u -channel which enter χ PT at next-to-leading order. In view of these differences one can be satisfied with the agreement and conclude that the numerically most important corrections from the χ PT point of view are included in our approach. At larger energies pure χ PT ceases to work and resummations must be incorporated in one or the other way [50, 23, 52, 12, 43].

Finally we show in Fig. 9 the result of a tree-level calculation based on our amplitudes (14). Obviously the charged-pion channel is fairly insensitive to rescattering effects, i.e. to a large extent dominated by the one-pion exchange, which is responsible for the steep rise of the cross section at low energies. The neutral-pion channel, however, which does not have the corresponding one-pion exchange, is dominated by loop/rescattering

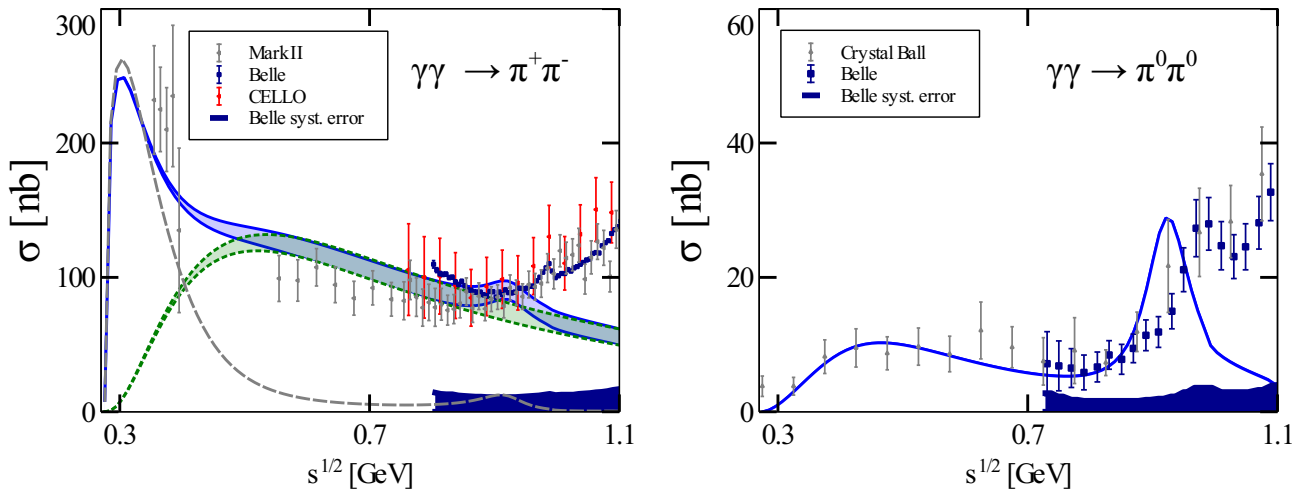


Fig. 6 Cross section for the reactions $\gamma\gamma \rightarrow \pi^+\pi^-$ (left) and $\gamma\gamma \rightarrow \pi^0\pi^0$ (right) using (28), (29) together with $g_5 \in [-5, 5]$. The obtained region is limited by the full thick lines. For the charged pions (left) the S-wave (long-dashed) and D-wave (short-dashed) are shown separately. See the figure caption of Fig. 3 for more details.

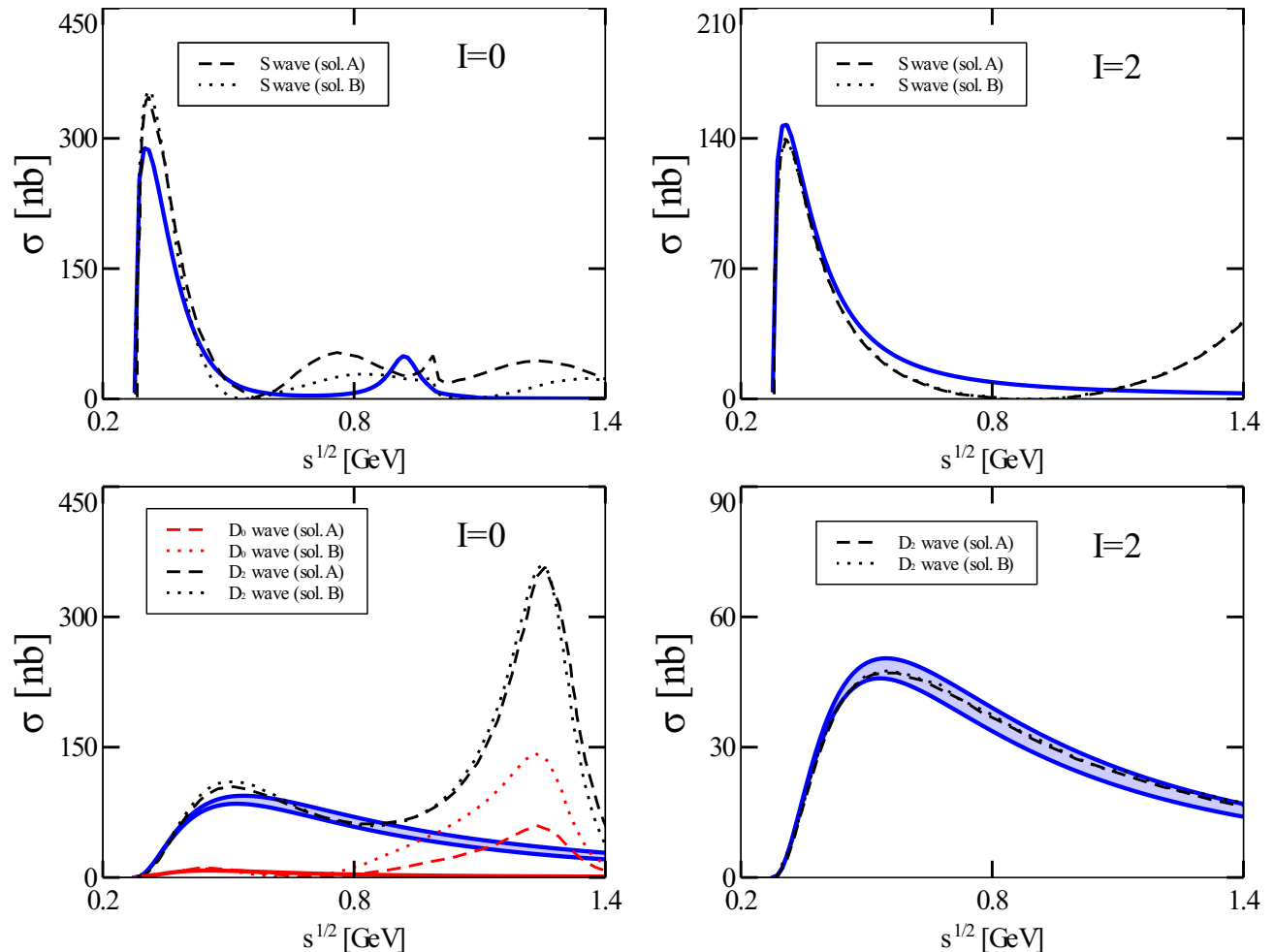


Fig. 7 Comparison of our results (solid lines) with the results of [1] for S-wave (top panels) and D-waves (bottom panels) and for different isospin (left panels: $I = 0$; right panels: $I = 2$). The subscript for the D-waves denotes the helicity. According to [1] two solutions have been obtained: solution A (dashed) is favored by a χ^2 fit, while solution B (dotted) is at the edge of acceptability.

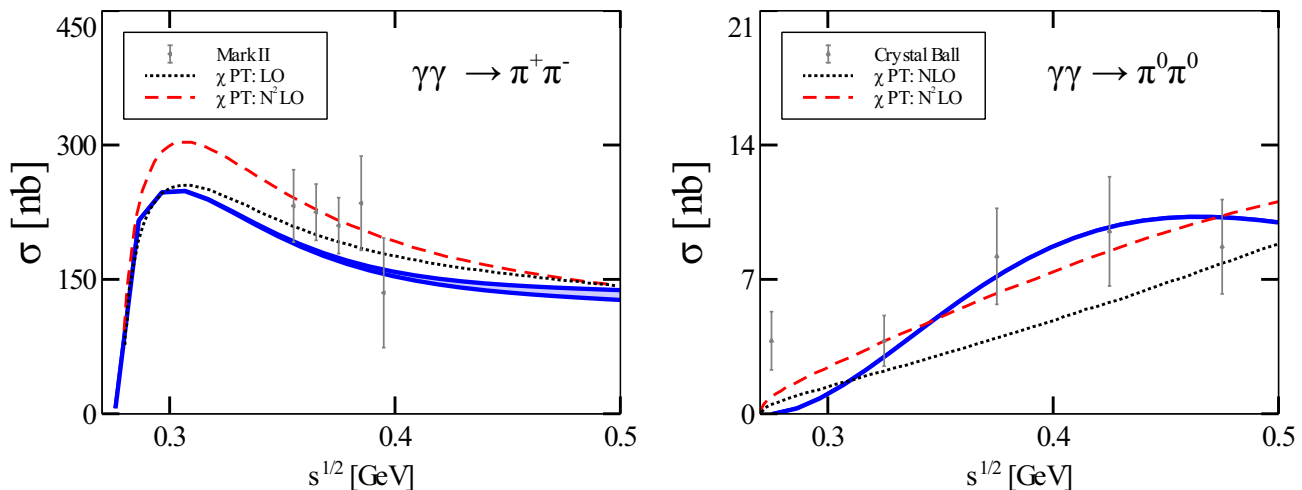


Fig. 8 Comparison of our results (full lines) to the calculations from chiral perturbation theory (χ PT) and to data. The dashed lines denote the next-to-next-to-leading-order calculations. The dotted lines denote the respective lowest-order non-trivial χ PT result, which is leading order for the charged case and next-to-leading order for the neutral case. See also the figure caption of Fig. 3 for more details.

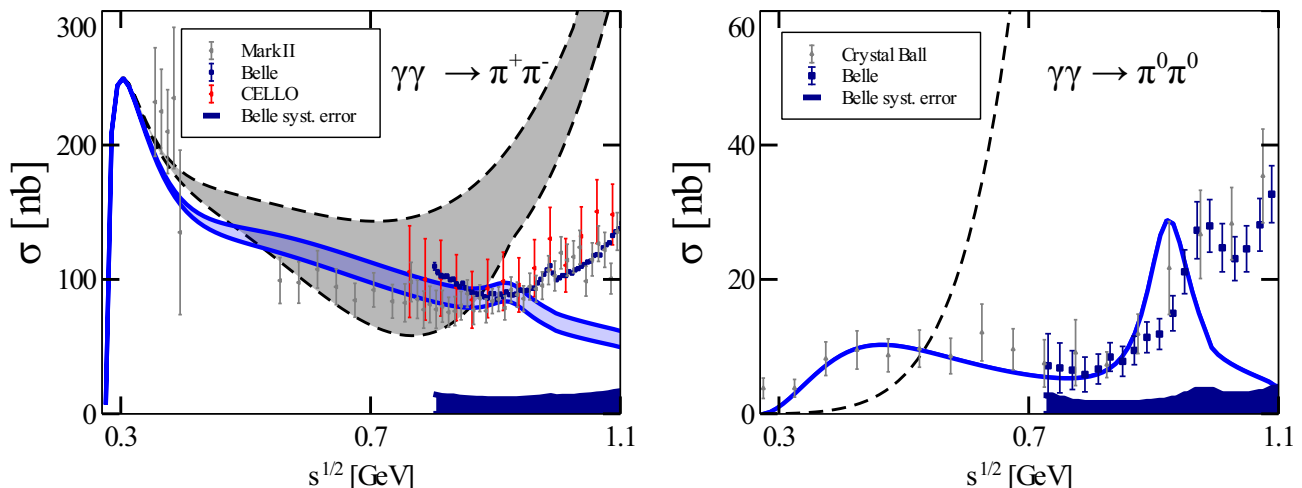


Fig. 9 Comparison of tree-level calculations to the full results and to data. Tree-level calculations are depicted by dashed lines. See also the figure caption of Fig. 3 for more details.

effects. In this channel the tree-level calculation fails already at low energies.

While the previously discussed channels have been used to some extent to fix our free parameters, the channels which we discuss in the following are pure predictions. Unfortunately the data situation is rather poor in all three channels $\gamma\gamma \rightarrow K^+K^-$, $K^0\bar{K}^0$ and $\eta\eta$, but we will see that it is a non-trivial task to match the available data points. We restrict ourselves to the energy region close to threshold, i.e. to $\sqrt{s} \leq 1.2$ GeV. There we expect the S-wave to dominate such that we do need to worry about the tensor mesons.

The reaction $\gamma\gamma \rightarrow K^+K^-$ is depicted in the top left panel of Fig. 10. Other theory approaches have been reported in [23, 53, 54]. Unfortunately there is only one

data point with a large energy uncertainty in the considered energy interval. Nonetheless, this data point is significantly lower than generic tree-level calculations. For comparison we show two types of such tree-level calculations. The dashed line is obtained if our Lagrangian is used directly for the amplitude and not for the potential of the full coupled-channel calculation. An alternative tree-level approach is to use just the kaon-exchange Born diagrams. We recall that the corresponding pion-exchange Born diagrams are very significant for the low-energy part of the reaction $\gamma\gamma \rightarrow \pi^+\pi^-$. (This is the χ PT-LO curve of Fig. 8.) For the kaon case the situation is obviously different. While tree-level calculations fail to reproduce even the close-to-threshold data, our full coupled-channel approach leads to a significant reduc-

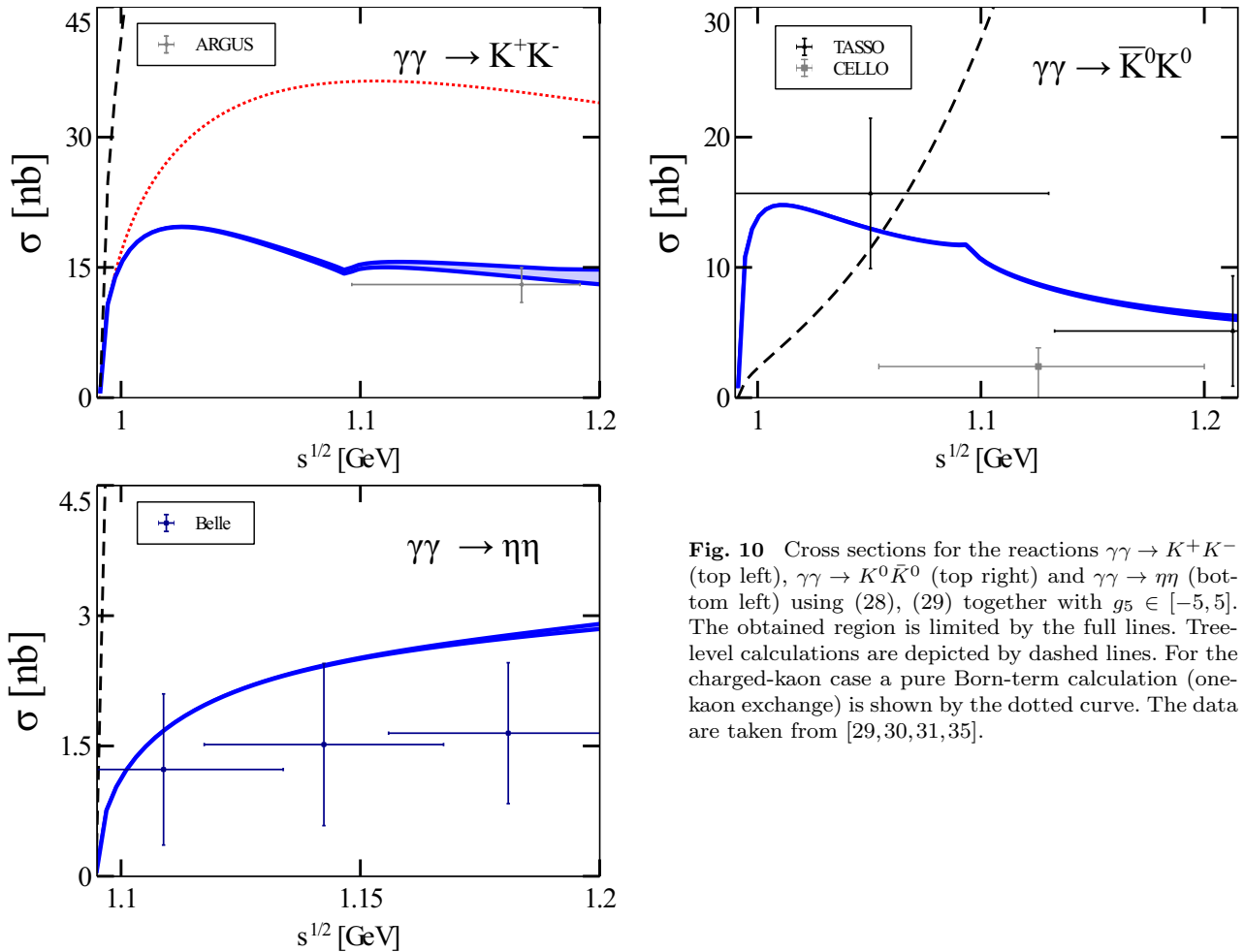


Fig. 10 Cross sections for the reactions $\gamma\gamma \rightarrow K^+K^-$ (top left), $\gamma\gamma \rightarrow K^0\bar{K}^0$ (top right) and $\gamma\gamma \rightarrow \eta\eta$ (bottom left) using (28), (29) together with $g_5 \in [-5, 5]$. The obtained region is limited by the full lines. Tree-level calculations are depicted by dashed lines. For the charged-kaon case a pure Born-term calculation (one-kaon exchange) is shown by the dotted curve. The data are taken from [29,30,31,35].

tion of the Born amplitude and matches the available data point very nicely. Hence, the final-state interactions are strong in this channel. A similar finding has been reported in [23]. Finally we note that our approach shows a visible cusp at the two-eta threshold. It is even more pronounced in the neutral-kaon channel to which we turn next.

The reaction $\gamma\gamma \rightarrow K^0\bar{K}^0$ is shown in the top right panel of Fig. 10. The data, albeit with large error bars, point to an initial step increase of the cross section with energy followed by a not so rapid fall. This behavior is qualitatively reproduced by our full calculation, though we do not fully match the second data point quantitatively. Tree-level calculations cannot reproduce at all this rise-and-fall behavior. Indeed, it is natural to expect that final-state interactions are strong because the photons couple stronger to the intermediate charged states than to the final neutral ones.

The bottom panel of Fig. 10 shows the cross section for the reaction $\gamma\gamma \rightarrow \eta\eta$ (see also [54]). The data suggest a rather flat energy dependence which cannot

be reproduced by a pure tree-level calculation (dashed line). In contrast, our full calculation (full lines) including rescattering meets this requirement of a comparatively flat cross section.

We stress again that our results for the two-eta and two-kaon channels are pure predictions. These channels did not enter the determination of free parameters. Note also that the results are basically insensitive to the remaining free parameter g_5 . Clearly, better data in these channels would be highly welcome to further check the validity of our coupled-channel approach with dynamical vector mesons.

6 Summary and outlook

We have performed a controlled study of the reactions $\gamma\gamma \rightarrow \pi^0\pi^0, \pi^+\pi^-, K^0\bar{K}^0, K^+K^-, \eta\eta$ and $\pi^0\eta$ in the energy regime between the respective thresholds and about 1.2 GeV. The reaction amplitudes were derived from the chiral Lagrangian with dynamical vector me-

son fields properly constrained by micro-causality and coupled-channel unitarity.

There are 5 unknown parameters, which have been constrained from the reactions $\gamma\gamma \rightarrow \pi^0\pi^0$, $\pi^+\pi^-$, $\pi^0\eta$ and from the differential decay $\eta \rightarrow \pi^0\gamma\gamma$. In particular we have achieved an excellent description of the reaction $\gamma\gamma \rightarrow \pi^0\eta$ with its lowest-lying scalar-isovector $a_0(980)$ resonance. The $a_0(980)$ resonance peak position does not depend on any of the free parameters. Based on our parameter constraints we predict the low-energy $\gamma\gamma \rightarrow K^+K^-$, $K^0\bar{K}^0$ and $\eta\eta$ cross sections.

While the vector mesons do play a crucial role in the derivation of the generalized potentials for $\gamma\gamma \rightarrow PP$ and $PP \rightarrow PP$ with $P = \pi, K, \eta$, the feedback of $PP \rightarrow PV$, VV reactions with $V = \rho, \omega, K^*, \phi$ remains to be studied systematically. According to the hadrogenesis conjecture we expect a quantitative description of the reactions $\gamma\gamma \rightarrow \pi^0\pi^0$, $\pi^+\pi^-$, $K^0\bar{K}^0$, K^+K^- , $\eta\eta$ and $\pi^0\eta$ up to about 2 GeV once such channels are incorporated in a controlled manner.

Accurate low-energy photon fusion data in particular in the strangeness channels would further scrutinize the intricate three-flavour dynamics of the Goldstone bosons and light vector mesons.

Acknowledgements The work of CT and SL has been supported by the European Community Research Infrastructure Integrating Activity ‘‘Study of Strongly Interacting Matter’’ (HadronPhysics3, Grant Agreement No. 283286) under the Seventh Framework Programme of the EU.

References

1. M.R. Pennington, T. Mori, S. Uehara, Y. Watanabe, *Eur. Phys. J. C* **56**, 1
2. J.A. Oller, L. Roca, *Eur. Phys. J. A* **37**, 15
3. R. Garcia-Martin, B. Moussallam, *Eur. Phys. J. C* **70**, 155
4. M. Hoferichter, D.R. Phillips, C. Schat, *Eur. Phys. J. C* **71**, 1743
5. Y. Mao, X.G. Wang, O. Zhang, H. Zheng, Z.Y. Zhou, *Phys. Rev. D* **79**, 116008
6. J. Gasser, M.A. Ivanov, M.E. Sainio, *Nucl. Phys. B* **745**, 84 (2006)
7. J. Gasser, M.A. Ivanov, M.E. Sainio, *Nucl. Phys. B* **728**, 31
8. J. Bijnens, F. Cornet, *Nucl. Phys. B* **296**, 557
9. J.F. Donoghue, B.R. Holstein, Y.C. Lin, *Phys. Rev. D* **37**, 2423
10. A. Gasparyan, M.F.M. Lutz, *Nucl. Phys. A* **848**, 126
11. I.V. Danilkin, A.M. Gasparyan, M.F.M. Lutz, *Phys. Lett. B* **697**, 147
12. I.V. Danilkin, L.I.R. Gil, M.F.M. Lutz, *Phys. Lett. B* **703**, 504
13. A.M. Gasparyan, M.F.M. Lutz, B. Pasquini, *Nucl. Phys. A* **866**, 79
14. M.F.M. Lutz, E.E. Kolomeitsev, *Found. Phys.* **31**, 1671 (2001)
15. M.F.M. Lutz, E.E. Kolomeitsev, *Nucl. Phys. A* **730**, 392
16. M.F.M. Lutz, E.E. Kolomeitsev, C.L. Korpa, *Prog. Theor. Phys. Suppl.* **156**, 51 (2004)
17. M.F.M. Lutz, E.E. Kolomeitsev, *Nucl. Phys. A* **755**, 29 (2005)
18. M.F.M. Lutz, M. Soyeur, *Nucl. Phys. A* **813**, 14 (2008)
19. M.F.M. Lutz, S. Leupold, *Nucl. Phys. A* **813**, 96
20. C. Terschläsen, S. Leupold, M.F.M. Lutz, arXiv:1204.4125 [hep-ph]
21. G. Ecker, J. Gasser, A. Pich, E. de Rafael, *Nucl. Phys. B* **321**, 311
22. B. Kubis, U.G. Meissner, *Nucl. Phys. A* **679**, 698
23. J.A. Oller, E. Oset, *Nucl. Phys. A* **629**, 739
24. M.F.M. Lutz, I. Vidana, *Eur. Phys. J. A* **48**, 124
25. J. Boyer, et al., *Phys. Rev. D* **42**, 1350
26. H. Behrend, et al., CELLO Collaboration, *Z. Phys. C* **56**, 381
27. H. Marsiske, et al., Crystal Ball Collaboration, *Phys. Rev. D* **41**, 3324
28. D. Antreasyan, et al., Crystal Ball Collaboration, *Phys. Rev. D* **33**, 1847
29. H. Albrecht, et al., ARGUS Collaboration, *Z. Phys. C* **48**, 183
30. H.J. Behrend, et al., CELLO Collaboration, *Z. Phys. C* **43**, 91
31. M. Althoff, et al., TASSO Collaboration, *Z. Phys. C* **29**, 189
32. S. Uehara, et al., Belle Collaboration, *Phys. Rev. D* **79**, 052009
33. T. Mori, et al., Belle Collaboration, *J. Phys. Soc. Jap.* **76**, 074102
34. S. Uehara, et al., Belle Collaboration, *Phys. Rev. D* **80**, 032001
35. S. Uehara, et al., Belle Collaboration, *Phys. Rev. D* **82**, 114031
36. S. Prakhov, eConf **C070910**, 159 (2007)
37. S. Prakhov, et al., *Phys. Rev. C* **78**, 015206
38. M. Unverzagt, Crystal Ball at MAMI Collaboration, *Nucl. Phys. Proc. Suppl.* **198**, 174
39. S. Leupold, M.F.M. Lutz, *Eur. Phys. J. A* **39**, 205
40. C. Terschläsen, S. Leupold, *Phys. Lett. B* **691**, 191
41. V.B. Berestetskii, E. Lifshitz, L.P. Pitaevskii, *Quantum Electrodynamics* (Pergamon Press, 1982)
42. D. Varshalovich, A. Moskalev, V. Khersonskii, *Quantum Theory of Angular Momentum* (World Scientific, Singapore, 1988)
43. I.V. Danilkin, M.F.M. Lutz, arXiv:1208.2568 [hep-ph]
44. G.F. Chew, S. Mandelstam, *Phys. Rev.* **119**, 467
45. K. Nakamura, et al., *J. Phys. G* **37**, 075021
46. K. Lalwani, Measurement of the branching ratio of a rare decay $\eta \rightarrow \pi^0\gamma\gamma$ with WASA-at-COSY. Ph.D. thesis, Department of Physics, Indian Institute of Technology Bombay (2010)
47. L. Ametller, J. Bijnens, A. Bramon, F. Cornet, *Phys. Lett. B* **276**, 185
48. E. Oset, J.R. Pelaez, L. Roca, *Phys. Rev. D* **67**, 073013
49. E. Oset, J.R. Pelaez, L. Roca, *Phys. Rev. D* **77**, 073001
50. J.A. Oller, E. Oset, *Nucl. Phys. A* **620**, 438
51. M. Doring, U.G. Meissner, E. Oset, A. Rusetsky, *Eur. Phys. J. A* **47**, 139
52. A. Gomez Nicola, J.R. Pelaez, *Phys. Rev. D* **65**, 054009
53. N.N. Achasov, G.N. Shestakov, *Phys. Usp.* **54**, 799
54. C.H. Lee, H. Yamagishi, I. Zahed, *Nucl. Phys. A* **653**, 185